



Masullo, A., & Theunissen, R. (2017). On the applicability of numerical image mapping for PIV image analysis near curved interfaces. *Measurement Science and Technology*, 28(7), [075301]. <https://doi.org/10.1088/1361-6501/aa6c8f>

Publisher's PDF, also known as Version of record

License (if available):  
CC BY

Link to published version (if available):  
[10.1088/1361-6501/aa6c8f](https://doi.org/10.1088/1361-6501/aa6c8f)

[Link to publication record in Explore Bristol Research](#)  
PDF-document

This is the final published version of the article (version of record). It first appeared online via IOP at <http://iopscience.iop.org/article/10.1088/1361-6501/aa6c8f/meta>. Please refer to any applicable terms of use of the publisher.

## University of Bristol - Explore Bristol Research

### General rights

This document is made available in accordance with publisher policies. Please cite only the published version using the reference above. Full terms of use are available:  
<http://www.bristol.ac.uk/pure/about/ebr-terms>

## On the applicability of numerical image mapping for PIV image analysis near curved interfaces

This content has been downloaded from IOPscience. Please scroll down to see the full text.

2017 Meas. Sci. Technol. 28 075301

(<http://iopscience.iop.org/0957-0233/28/7/075301>)

View [the table of contents for this issue](#), or go to the [journal homepage](#) for more

Download details:

IP Address: 137.222.138.50

This content was downloaded on 06/07/2017 at 13:46

Please note that [terms and conditions apply](#).

You may also be interested in:

[Iterative image deformation methods in PIV](#)

F Scarano

[Image pre-processing method for near-wall PIV measurements over moving curved interfaces](#)

L C Jia, Y D Zhu, Y X Jia et al.

[Correlation mapping method in PIV analysis](#)

J Chen and J Katz

[An adaptive sampling and windowing interrogation method in PIV](#)

R Theunissen, F Scarano and M L Riethmuller

[PIV uncertainty quantification by image matching](#)

Andrea Sciacchitano, Bernhard Wieneke and Fulvio Scarano

[An extended study of a generalized DPIV processing technique](#)

J Duncan, T Bryce, H Thomsen et al.

[Collaborative framework for PIV uncertainty quantification: comparative assessment of methods](#)

Andrea Sciacchitano, Douglas R Neal, Barton L Smith et al.

[Image-preprocessing method for near-wall particle image velocimetry \(PIV\) image interrogation with very large in-plane displacement](#)

Yiding Zhu, Huijing Yuan, Chuanhong Zhang et al.

[Uncertainty on PIV mean and fluctuating velocity due to bias and random errors](#)

Brandon M Wilson and Barton L Smith

# On the applicability of numerical image mapping for PIV image analysis near curved interfaces

**Alessandro Masullo and Raf Theunissen**

Department of Aerospace Engineering, University of Bristol, Bristol, United Kingdom

E-mail: [a.masullo@bristol.ac.uk](mailto:a.masullo@bristol.ac.uk)

Received 17 October 2016, revised 3 April 2017

Accepted for publication 11 April 2017

Published 2 June 2017



## Abstract

This paper scrutinises the general suitability of image mapping for particle image velocimetry (PIV) applications. Image mapping can improve PIV measurement accuracy by eliminating overlap between the PIV interrogation windows and an interface, as illustrated by some examples in the literature. Image mapping transforms the PIV images using a curvilinear interface-fitted mesh prior to performing the PIV cross correlation. However, degrading effects due to particle image deformation and the Jacobian transformation inherent in the mapping along curvilinear grid lines have never been deeply investigated. Here, the implementation of image mapping from mesh generation to image resampling is presented in detail, and related error sources are analysed. Systematic comparison with standard PIV approaches shows that image mapping is effective only in a very limited set of flow conditions and geometries, and depends strongly on *a priori* knowledge of the boundary shape and streamlines. In particular, with strongly curved geometries or streamlines that are not parallel to the interface, the image-mapping approach is easily outperformed by more traditional image analysis methodologies invoking suitable spatial relocation of the obtained displacement vector.

Keywords: CFD mesh, image mapping, PIV, vector relocation, adaptivity

(Some figures may appear in colour only in the online journal)

## 1. Introduction

Particle image velocimetry (PIV) has become a well-established measurement technique to evaluate the underlying flow field from experimental flow images. The most common analysis process involves the subdivision of pairs of consecutive images into sub-areas, typically referred to as correlation or interrogation windows, and subsequently estimating the displacement of the particle images captured within these areas by means of statistical operators such as cross-correlation (Adrian 1991). To increase the accuracy of the obtained displacements beyond pixel level, sub-pixel resolution is achieved by Gaussian fitting of the correlation peak (Westerweel 1997). Detrimental

effects of displacement gradients on accuracy are then counteracted through iterative multi-grid approaches (Scarano and Riethmuller 2000) incorporating image deformation.

Although very versatile and widely used, it is well recognised that cross-correlation based techniques only provide robust and reliable measurements in interrogation areas free of interfaces or boundaries. Both the decrease in number of particle images contributing to the correlation and the presence of strong light reflections close to interface degrade cross-correlation performances (Keane and Adrian 1992). This problem has been extensively addressed in literature with a variety of proposed attempts to minimise reflections in the image recording stage. Among such solutions are the use of fluorescent paint, electropolished materials or transparent media (Paterna *et al* 2013). Nevertheless, ideal experimental settings are not always possible and reliable data must still be extracted from images acquired in such non-perfect



Original content from this work may be used under the terms of the [Creative Commons Attribution 3.0 licence](https://creativecommons.org/licenses/by/3.0/). Any further distribution of this work must maintain attribution to the author(s) and the title of the work, journal citation and DOI.

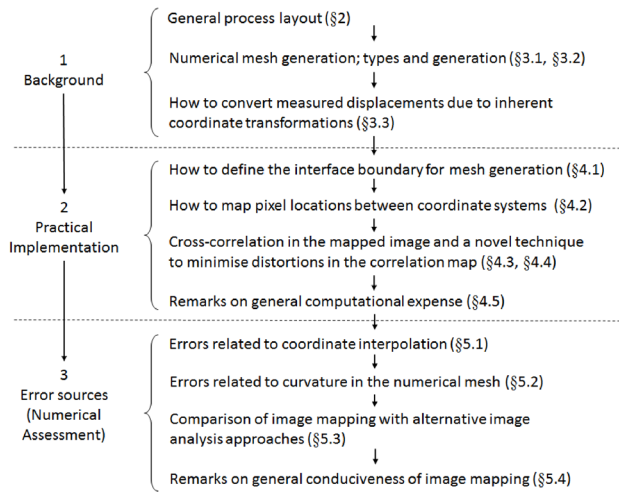


**Figure 1.** Three tier structure of the manuscript with accompanying paragraph numbering.

conditions. For this reason in the last decade effort has been spent on the algorithmic side of PIV analyses. Some of the most common methods to reduce the effect of boundaries present is to adopt masking techniques to exclude identified image regions (Ronneberger *et al* 1998, Gui *et al* 2003). Masking techniques are often enhanced by an automatic vector relocation based on the centroid of the truncated correlation window (Usera *et al* 2004) such that the new vector location offers a more representable attribution of local seeding displacement. A different approach followed by Tsuei and Savaş (2000) consists in mirroring particle images located within the flow region across interfaces, reducing the detrimental effects on the correlation map. However, the inherent displacement errors will strongly be related to the velocity field curvature and degree of overlap between the correlation windows and mirrored interface. To circumvent such a dependency on mutual overlap between the interface and correlation window Theunissen *et al* (2006) introduced the concept of adapting both the location and aspect ratio of the correlation windows to the presence of interfaces. Overlap between correlation windows and interfaces was minimized by adjusting the position, orientation and size of the windows leading to drastic improvements in spatial resolution.

A completely alternative approach, which is the case study of this paper, involves the distortion of correlation windows by means of image mapping to follow the interface geometry, thus completely avoiding the capture of interfaces within correlation windows. Image mapping techniques usually perform a transformation of the images in a logical space in which the problem of matching particle images patterns is solved. Ruan *et al* (2001) adopted this methodology to directly evaluate vorticity. In their study, particle images were deformed through a Cartesian to polar transformation and processed through cross-correlation, allowing the explicit deduction of vorticity. A similar image mapping was used to deform images in the near vicinity of a wavy wall through curvilinear coordinate transformations (Nguyen *et al* 2010), followed by a 1D method of estimation of the wall friction velocities by means of ensemble correlation of interrogation windows one

pixel in height. Similarly, Jeon and Sung (2011) and Park *et al* (2015) used textons to track a free surface, from which regularized coordinates were generated to map the particle images into a straight interface.

Despite the apparently successful use of image mapping in previous works, both an in-depth analysis of the inherent parameters defining the image mapping and a comparison with traditional cross-correlation has to the best of the authors' knowledge never been presented. Moreover, all studies mentioned consider only imaged sections of interfaces whereas common aeronautical applications may involve more strongly curved geometries captured in their entirety such as e.g. aerofoils. The aim of this paper is therefore to fill this lack by documenting and investigating the individual stages in the image mapping process and study the generality of image mapping for PIV applications from the generation of the body-conforming mesh for a generic surface of interest, to the effects of the deformation on the cross-correlation map and related displacement measurements. Possible error sources involved in each stage of the process are scrutinized and assessed with synthetic images in order to provide the reader with a complete understanding of the image mapping method.

The paper has an underlying three-tiered structure. To aid the reader an overview of the objectives of each tier is provided in figure 1. The general concept underlying image mapping and its location within typical image analysis processes are discussed in section 2. Section 3 provides further background information regarding image mapping by addressing the mathematical aspects behind numerical mesh generation and the necessary re-scaling of obtained particle image displacement estimates. The second tier of the paper focusses on the practical aspects of image mapping, starting with the generation a general continuous body-fitted mesh from a typical, pixelised, user-defined mask. After presenting the adopted interpolation method for the involved coordinate transformations, the appropriate correlation window sizing and cross-correlation operation are discussed. In the process of finding the limits of applicability of image mapping, the authors set out to find optimal solutions that minimises the errors involved in each stage of method. The authors accordingly present a novel technique to minimise distortions in the cross-correlation maps due to deformed particle images caused by the inherent image transformations. This however comes at the expense of computational cost which is discussed in section 4.5. In the final section the authors present a thorough and detailed error analysis based on computer generated PIV images for each of the key stages in image mapping. Error sources caused by the coordinate transformation and curvature in the generated numerical mesh are highlighted. Since the benefits of image mapping were already shown in the existing literature, the aim of the current paper is more focused on the analysis of the limits of the image mapping method which are encountered in the study of strongly curved surfaces. For this reason simulated PIV images of the flow over a Joukowsky airfoil are utilised when juxtaposing the performances of image mapping with standard PIV and advanced adaptive approaches. Here understanding the real advantages of such a mapping technique for PIV is pursued. Even when combining image

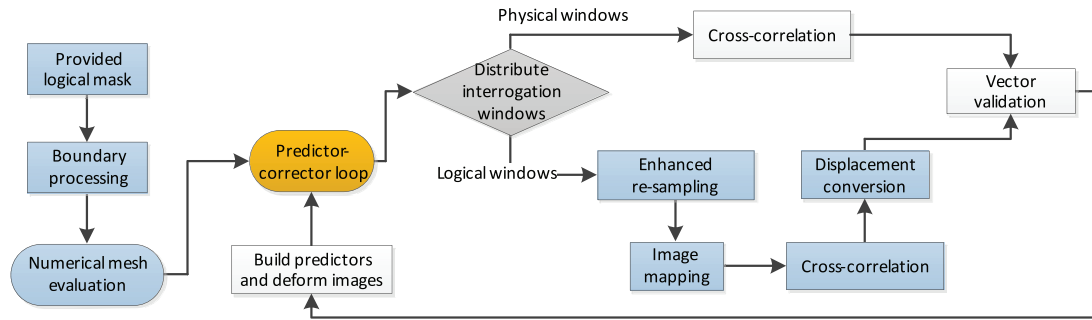


Figure 2. Description of the iterative algorithm.

mapping with adaptive approaches in attempts to maximise the performances of image mapping, no distinct ameliorations were achieved. It will be shown instead that the problem of affected image quality due to the deformation of image mapping constitutes one of the strongest sources of error. In section 5.4 the authors therefore present general remarks on the applicability of image mapping, in which the reader will be discouraged from the use of such a technique. Instead it is argued that more conventional image analysis methodologies are more reliable and robust.

## 2. Problem definition and general image mapping methodology

Robustness of cross-correlation of interrogation areas in proximity of curvy surfaces is hampered not only due to flow-induced effects, such as stronger gradients in velocities, but also stronger dissemblance of the image recording from the ideal<sup>1</sup> condition due to optical degradations. The latter mainly constitutes light reflections and a truncation in PIV signal related to the reduction in particle seeding density across the interface (Theunissen *et al* 2008a). Dedicated image routines are therefore needed to ensure cross-correlation operations will retain sufficiently high signal-to-noise ratios and safeguard accuracy.

One possible means is to avoid any overlap between cross-correlation windows and interfaces entirely. To this extent a numerical boundary-fitted mesh originated from a mask of the curvy surface can be generated. The user-defined binary mask indicates the location of the objects within the image recording and is used as a boundary condition for a system of partial derivative equations (PDE) defining the body-conforming coordinate system. The solution to these equations generates a discrete set of points representing the transformation from the physical plane, i.e. the original images, to a computational plane. Original images are subsequently transformed such that the curvilinear mesh in the logical plane is represented as a rectilinear one. Here the surface becomes a straight line and correlation windows aligned with this straight boundary can be imposed such that any interface overlap is avoided.

In ideal conditions (e.g. when the interface geometry exhibits a high curvature radius and a low spatial deformation), the transformed images can be suitably analysed

by standard PIV image analyses routines as suggested by Nguyen *et al* (2010). Interfaces characterized by strong curvatures on the other hand may introduce additional deformations of the correlation map. As will be shown in section 5.2, these degrading effects may even outweigh image mapping's potential benefit of avoiding the overlap with the interface. In order to push image mapping to its limits and achieve optimal measurements, the method may be further extended through combinations with an adaptive spatial sampling (Theunissen *et al* 2008b) as assessed in section 5.3. Previous works in literature show that the spatial resolution near interfaces can be improved by means of adapting the spatial distribution of correlation windows and their size on the basis of identified flow features (Theunissen *et al* 2006) or to the presence of interfaces (Theunissen *et al* 2008b). It should be noted that such adaptive image interrogation processes adopting image mapping are already quite advanced with added degrees of complexity. However, the authors have considered such state-of-the-art approaches in this manuscript to allow an objective assessment of potential advantages of image mapping in PIV analyses. The adaptive approach adopted in the current work allows an automatic selection of the window properties such that correlation windows are automatically reduced in size towards the interface. After this stage correlation windows are divided into two categories depending on their distance from the identified surface. Those far away from the surface will be straightforwardly processed with cross-correlation, whereas those in vicinity of the curvy surface will be deformed one by one using the numerical mapping and converted back into physical displacements. The basic idea behind this approach can be summarized by what in CFD analysis is known as the Chimera approach (Steger 1991).

A flowchart of the general image interrogation methodology is presented in figure 2. The overall layout remains analogous to the classical iterative predictor-corrector scheme with refinement of window sizes presented by Scarano and Riethmuller (2000). Once interrogation windows are distributed adaptively across the image, cross-correlation is performed utilising either pixel intensities of the original image or re-interpolated grey levels according the numerical mesh transformation. The latter requires additional operations which will be elucidated in section 4.3. Sub-pixel accuracy is achieved with a nine-points 2D Gaussian regression expressed in an explicit formulation (Nobach and Honkanen 2005) capable of dealing with potentially deformed correlation peaks as a result of non-linear image mapping. Displacements evaluated

<sup>1</sup> The ideal image consists of uniformly distributed bright particle images superimposed onto a black background.



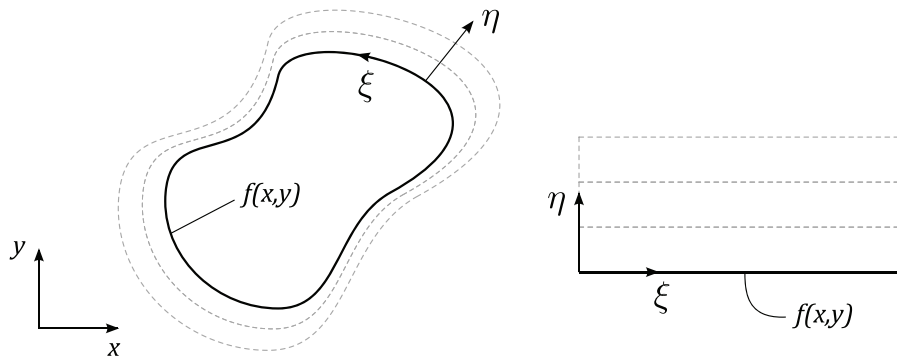


**Figure 3.** Illustration of the concept of image mapping. (left) Curvilinear coordinates  $(\xi, \eta)$  are fitted in the physical plane to the object with boundary condition  $f(x, y)$ . (right) The curved interface becomes a straight line after transformation into the logical plane.

on mapped images are subsequently converted back on to the physical plane by means of the Jacobian (obtained from the PDEs), merged with physical displacement vectors obtained through traditional methodologies and validated using a non-structured vector validation routine (Masullo and Theunissen 2016). The scattered displacements are interpolated on a pixel-wise grid by means of natural neighbours interpolation (Bobach *et al* 2009) to provide a predictor for iterative image deformation (Scarano 2002) and further reduce the effects of velocity gradients.

The incorporation of the numerical mesh-based image mapping and adaptive correlation window localisation thus constitutes additional processing steps within a standard PIV analysis. In the remainder of this paper it is the concept of image mapping near strongly curved geometries and the analysis of the associated measurement errors that will be the subject of investigation.

### 3. Mathematical background of body-conforming image mapping

Prior to presenting the mathematical background underpinning the coordinate transformations constituting image mapping, some pivotal definitions used throughout this paper are outlined to improve clarity. The plane defined by spatial coordinates  $(x, y)$  will represent the physical plane which is equivalent to the captured PIV images expressed in terms of recorded pixel coordinates. The  $(\xi, \eta)$  plane is defined as the mapped or logical plane, where  $\xi$  and  $\eta$  are the curvilinear coordinates attributed to the angular and radial directions respectively. It is on this plane that the original image recordings will be transformed as per figure 3. The Chimera area then refers to the finite extent of the numeric mesh on the physical plane, which is the only part of the image transformed and analysed on the logical plane (see also figure 15 for an illustration).

#### 3.1. Hyperbolic versus elliptic mesh

Numerical meshes in computational fluid dynamics (CFD) are used to discretize the non-linear partial differential equations (PDEs) modelling the flow in order to allow the computation of an approximate solution. These meshes can be categorised as either structured or unstructured. While the

former is defined by the intersection of curvilinear coordinate surfaces, the latter lacks any relation between coordinate directions. The current intention is for the mapping to describe the spatial rearrangement of image intensities when altering reference coordinate systems. As digital images are composed of intensities defined in pixel elements which are already arranged in an array format, structured meshes are consequently the most suitable grid type.

The generation of a structured mesh can be performed through several approaches of which the most common constitute analytical transformations, algebraic schemes and other based on partial derivative equations (PDE). Details regarding numerical grid generation can be found in Thompson *et al* (1999) but it presently suffices to note that while analytical transformations are the fastest and most accurate, their use is limited to more simplistic analytical geometries such as cylinders, sinusoidal walls, etc. In view of the intended general applicability of image mapping these will be left out of consideration. Grid generation based on partial differential equations is typically slower than its algebraic counterpart but is the preferred choice in the present work as they offer a higher degree of mesh smoothness and can concomitantly be expected to minimise image artefacts caused by image mapping. In fact, algebraic meshes are based on transfinite interpolation and are more likely to result in overlapping of the boundaries (Thompson *et al* 1999)

The numerical mesh is a discrete set of curvilinear coordinates  $(\xi, \eta)$  satisfying either an elliptic or hyperbolic system of PDE equations. Independent of their classifications, these equations describe the coordinate transformations when alternating between the physical  $(x, y)$  and logical  $(\xi, \eta)$  plane. Elliptic meshes are obtained by solving the system of elliptic equations presented in equation (1) through iterative schemes based on finite differences. The equation of this mesh comes from an analogy to a stretching membrane attached to the boundary of the object. These meshes are perfectly suitable for closed domains, where all the boundary geometries are specified and are considered best in terms of smoothness (Thompson 1987):

$$\frac{\partial^2 \xi}{\partial x^2} + \frac{\partial^2 \xi}{\partial y^2} = 0 \text{ and } \frac{\partial^2 \eta}{\partial x^2} + \frac{\partial^2 \eta}{\partial y^2} = 0. \quad (1)$$

Starting from the object geometry identified in the image recordings, boundary conditions are provided in terms of

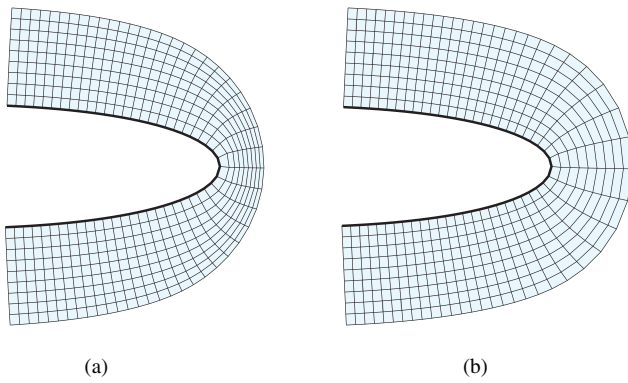


**Figure 4.** Solution of a hyperbolic mesh near the leading edge of an airfoil in case of (a) constant cell area, yielding an increasingly high cell-aspect ratio near the nose with radial distance and (b) adjusting the cell area proportional to the Jacobian. This reduces the numerical cell-aspect ratio and minimises artificial displacement gradients when mapping images according to the generated mesh.

$x$  and  $y$ . However, the solution to equation (1) expresses the unknown angular,  $\xi$ , and radial coordinates,  $\eta$ , as functions of the physical coordinates,  $x$  and  $y$ . System (1) is therefore usually rearranged such that the physical coordinates become the unknowns and the boundary condition can be defined with respect to the body geometry when  $\eta = 0$ , as illustrated in figure 3. An additional user-defined non-homogenous term can be added to the equations to promote special grid properties such as line spacing, orthogonality, etc.

Alternatively a hyperbolic system of partial differential equations forms the basis for the intended mesh generation. Here the equations are analogous to the description of waves transporting disturbances on water surfaces:

$$\frac{\partial x}{\partial \xi} \frac{\partial x}{\partial \eta} + \frac{\partial y}{\partial \xi} \frac{\partial y}{\partial \eta} = 0 \text{ and } \frac{\partial x}{\partial \xi} \frac{\partial y}{\partial \eta} - \frac{\partial y}{\partial \xi} \frac{\partial x}{\partial \eta} = \Delta A. \quad (2)$$

The first equality in (2) imposes orthogonality while the second controls the local cell area through  $\Delta A$ . Parameter  $\Delta A$  is user-defined and can subsequently take on any form;  $\Delta A = \text{constant}$ ,  $\Delta A = \Delta A(x, y)$  or  $\Delta A = \Delta A(\xi, \eta)$ . The solution methodology starts from the geometry of the boundary conditions and propagates outwards until a user-defined extent. For this reason, this type of mesh is more suitable for open domains.

It is important to note that when attempting to generate a body-conforming mesh to map PIV images, the purpose of the grid, and therefore its inherent characteristics, will be slightly different from those used in CFD. Computational fluid dynamics utilises the mesh to obtain a discrete solution of the underlying flow equations at every grid node, therefore, an accrual of mesh points in vicinity of the surface is beneficial to the estimate of velocity near the object. In the current work, instead, the mesh is used to deform images that are thereafter analysed in sub-areas to evaluate the displacement of particle images. The choice of optimal mesh characteristics should thus introduce the least amount of artificial displacement gradients in the logical plane as these are well-known to hinder reliable cross-correlation (Westerweel 2008). For this reason, the optimal mesh should maintain a constant node density independent of the distance from the boundary or its

curvature radius. When comparing elliptic and hyperbolic meshes, the former tends to automatically densify the number of points where surfaces have a lower radius of curvature and has the opposite behaviour where surfaces are smoother. This effect is to be avoided for image mapping purposes because of the aforementioned artificial gradients. Moreover, the iterative approach required to solve an elliptic system of partial differential equations renders the associated mesh generation slower compared to the hyperbolic type, where a faster marching technique can be adopted (Thompson *et al* 1999). These motivations lead the authors' grid choice to a hyperbolic mesh.

### 3.2. Hyperbolic mesh generation

Having identified hyperbolic meshes as most suitable for PIV image analyses, this section highlights aspects in the mesh generation which require careful consideration. Utilising the hyperbolic partial differential equations expressed in (2) and a complementary boundary condition describing the pixel locations  $(x, y)$  of the interface geometry in terms of logical coordinates  $(\xi, \eta)$ , the solution of the well-posed system of equations provides for each combination of curvilinear coordinates  $(\xi, \eta)$  the corresponding physical coordinates  $(x, y)$ . This constitutes the image mapping. In this work, the authors opted for a simple first-order explicit solver because of its low computational effort. Details on the solver are provided in the appendix. Although the problem expressed in (2) is closed, three more parameters must be specified to generate the desired mesh; the local cell area  $\Delta A$ , the wall-normal extent of the mesh and a smoothening factor. Maintaining a uniform cell area may be the most simplistic approach, yet it leads to severe stretching of the cell aspect ratio when increasing the radial extent of the mesh in regions of stronger boundary curvature as illustrated in figure 4(a). In section 5.2 the authors will show that such stretching introduces detrimental artificial displacement gradients in the mapping and should be categorically avoided. The area of the cells must therefore increase according to the spreading of the radial coordinate  $\eta$ . Here, an automatic adjustment of  $\Delta A$  to the transformation's tangential derivatives is proposed:

$$\Delta A = \Delta A(\xi, \eta) = \Delta A_0 \sqrt{\left(\frac{\partial x}{\partial \xi}\right)^2 + \left(\frac{\partial y}{\partial \xi}\right)^2} \quad (3)$$

with 0 designating the initial condition. The effect of altering the cell-area according to the local Jacobian is exemplified in figure 4(b). The reader should bear in mind that the illustrated mesh in figure 4 is representative of the subsequent image deformation and is not related to the sizing or positioning of interrogation windows.

The extent of the numerical mesh is defined by the user and should equal at least one initial correlation window size. The degree of grid smoothening must be selected considering the shape of the interface and is of pivotal importance both for numerical stability and mesh coherence. As an example, in absence of artificial smoothening, concave shaped interfaces are attributed meshes which intersect themselves as they propagate outwards. This creates a non-unique surjective transformation of the mesh as illustrated in figure 5(a).

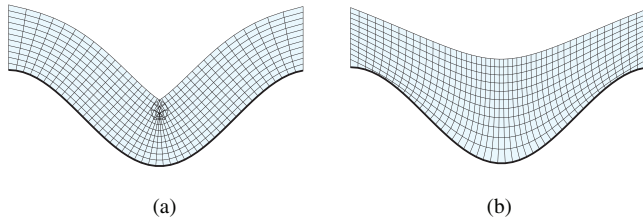


**Figure 5.** (a) Illustration of a self-intersecting mesh in case of concave boundary geometries without the application of artificial smoothing yielding non-unique image mapping and (b) the result of incorporating a smoothing factor.

Incorporation of artificial smoothing by means of adding an explicit second-order dissipation term to the right hand side of equation (2) as proposed by Chan and Steger (1992) renders a more conducive mapping (figure 5(b)).

### 3.3. Displacement conversion

When images will be transformed into the logical  $(\xi, \eta)$  plane and evaluated, corresponding particle image displacements  $d\xi$  and  $d\eta$  must be converted into physical displacements  $dx$  and  $dy$  in order to be meaningful. The transformation of logical displacements is achieved using the Jacobian  $[J]$  of the transformation, expressed by equation (4):

$$\begin{bmatrix} dx \\ dy \end{bmatrix} = \begin{bmatrix} \frac{\partial x}{\partial \xi} & \frac{\partial x}{\partial \eta} \\ \frac{\partial y}{\partial \xi} & \frac{\partial y}{\partial \eta} \end{bmatrix} \begin{bmatrix} d\xi \\ d\eta \end{bmatrix} = [J] \begin{bmatrix} d\xi \\ d\eta \end{bmatrix}. \quad (4)$$

Derivatives appearing in (4) are evaluated through an interpolation of the second-order finite differences of the physical coordinates  $(x, y)$  with respect to  $\xi$  and  $\eta$ .

## 4. Practical implementation of cross-correlation using body conforming numerical grids

### 4.1. Interface boundary definition

The generation of the numerical mesh starts from the boundary condition provided in the form of a logical binary image identifying the object. As a direct consequence of pixelisation, edges cannot be straightforwardly used as mesh boundary conditions but need to be properly smoothed and rearranged (figure 6). The process of boundary smoothing can be performed in different ways and several techniques have been tested among which Gaussian convolution, discrete cosine transform (Garcia 2010) and Fourier descriptors (Feudjio *et al* 2014). In spite of the number of the techniques tested, all smoothing functions applied to the mask edges produce artificial oscillations due to the non-random nature of the quantization error of the discrete pixel positions making up the interface boundary. In order to overcome this problem, the authors propose a line simplification algorithm rather than smoothing for which the Douglas–Peucker algorithm (Douglas and Peucker 1973) has been efficiently adopted.

The process of generating a boundary condition from the provided masking image for subsequent mesh generation is depicted in figure 6(b) and consists of four main steps. Edges are first extracted from the logical mask by means of classical edge

detection routines. Since the edge of the mask is made of discrete pixels the suggested algorithm simplifies the step-shaped curve by iteratively reducing the number of points and selecting subsets with the aim of attaining a difference between the original and sub-sampled edge below a defined threshold. Following a spline interpolation of the simplified edges to reconstitute the number of edge pixels, edge points are redistributed along the spline curve to be equidistant. The latter is of importance since a non-equally distributed mesh introduces artificial deformation into the mapped image, affecting the quality of the cross-correlation and therefore the displacement measurement accuracy. The number of points used to re-interpolate the simplified edge will affect the number of points of the mesh in the angular direction and consequently the accuracy of the transformation. For this reason the mesh density should be selected to ensure each image pixel is covered by at least one mesh node.

Another important aspect concerning the generation of the boundary conditions for a numeric mesh appertains the overall topology. The main obstacle is that the logical plane is always rectangular shaped. Although the transformation from a general shape to a rectangle can be quite straightforward (e.g. L- or C-shaped boundaries need only straightening) closed shapes need further attention. An annulus, for instance, cannot be transformed into a rectangular shape unless a branch cut is introduced on the physical plane. No general solution exists to overcome the inherent problem and the user is obliged to recursively adjust the mesh on a case-by-case basis to ensure continuity across the branch cut when interrogation windows overlap with it. Particular topological conditions could be needed also in case of shape singularities or strong curvature.

### 4.2. Interpolation of mesh coordinates

The hyperbolic numerical mesh is generated through the system of equations (2), which can be solved adopting e.g. the approach recorded in the appendix. Independent of the adopted solver, the obtained numerical solution consists of a discrete set of data points in the physical plane  $(x_{ij}, y_{ij})$ , which are located on the nodes of the numerical mesh and for which the corresponding equivalent in the logical plane  $(\xi_{ij}, \eta_{ij})$  is known. Figures 7(a) and (b) show an example of those discrete points in the form of a 3D surface for a simple sinusoidal mesh. It should be noted that the locations  $(\xi_{ij}, \eta_{ij})$  constitute the nodes of an equispaced rectangular grid and that the samples  $(x_{ij}, y_{ij})$  do not need to coincide with original pixel locations. As will be shown in section 4.3, cross-correlation in the logical plane however requires image intensities defined at a higher resolution, i.e. at locations between the available  $(\xi_{ij}, \eta_{ij})$  samples. The transformation between a general point on the logical  $(\xi, \eta)$  plane and the physical  $(x, y)$  plane thus requires an interpolation of the discrete point locations. In the current work the authors have adopted a quintic spline scheme (Astarita and Cardone 2004).

The inverse transformation from the physical plane to the logical plane, which is depicted in figures 7(c) and (d), is also performed through interpolation, although additional attention is required since the coordinates  $(\xi, \eta)$  are distributed on the nodes of the mesh on the physical plane and, as such, do not constitute a structured grid as required for spline



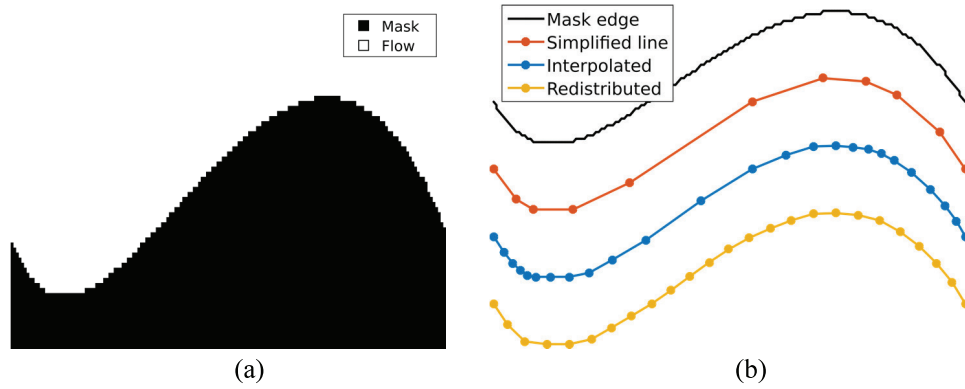


**Figure 6.** (a) A logical mask provided as an image, clearly illustrating the discrete nature of the boundary edge. (b) Processing of boundary points extracted from the edges of the mask as per the Douglas–Pecker line simplification algorithm.

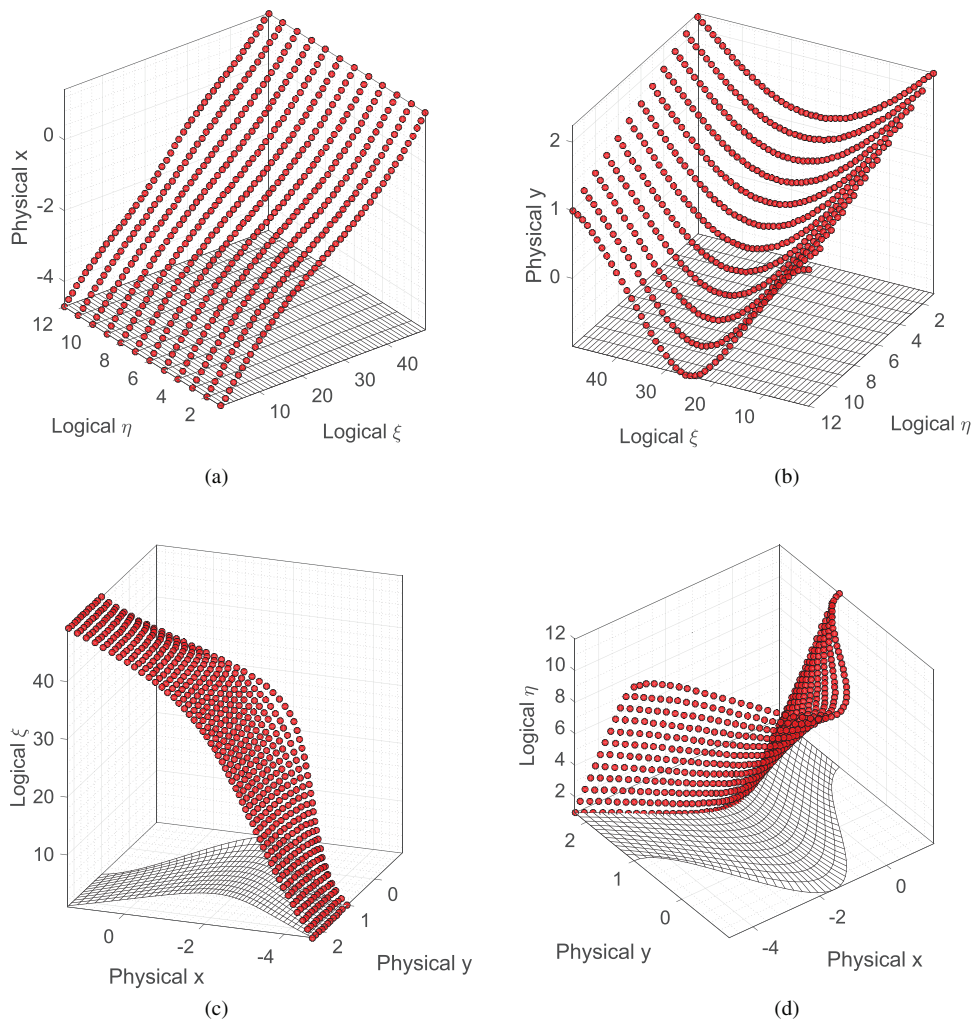


**Figure 7.** Plot of the coordinates mapping for the example mesh proposed in figure 5. (a) and (b) Physical coordinates plotted against structured logical coordinates. (c) and (d) Logical coordinates plotted against scattered physical coordinates.

interpolation. For this reason, a non-structured interpolant is needed and in this work, a natural neighbours interpolation (Bobach *et al* 2009) has been selected accordingly.

**4.3. Correlation in the logical plane and enhanced re-sampling**

Following the generation of the numerical mesh, interrogation window centres are distributed on the physical plane

and, in line with the Chimera approach, analysed differently according to their distance from the interface boundary (see section 2). Interrogation areas of which the centroid is located outside the numerical mesh are analysed directly by means of cross-correlation on the physical plane as per standard PIV. Correlation windows whose centroid falls within the boundary fitted mesh will utilise the logical plane, where rectangular correlation windows are constructed and analysed by means of standard cross-correlation.

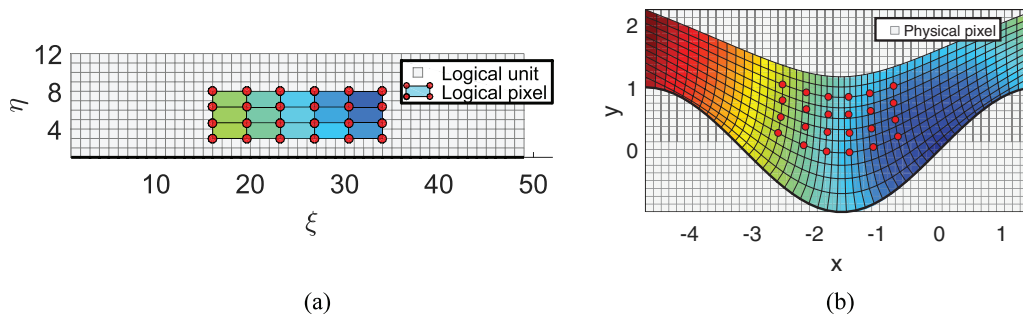


**Figure 8.** Description of the interpolation process of image intensities for correlation windows. (a) Logical pixels (filled rectangles bounded by red circles) are distributed on the logical plane. The grey grid represents the logical units. (b) The locations are mapped from the logical to the physical plane and image intensities on the physical plane are interpolated to yield the logical pixel intensities.

The relations established in section 4.2 describing image mapping between the different coordinate systems allow a complete reconstruction of the image recordings onto the logical plane. This is the common approach adopted in previous studies (Nguyen *et al* 2010, Jeon and Sung 2011, Park *et al* 2015), followed by cross-correlating intensities in the logical plane. However, digital images are not continuous but composed of discrete, square elements, i.e. physical pixels. Image mapping will consequently distort these pixel units. Due to the potentially strong non-linearity of the mesh shape and the consequent divergence (or convergence) of the radial lines in proximity of a curved surface, the use of a uniquely predefined correlation window size in the logical plane expressed in terms of physical pixels produces under-sampled (or over-sampled) particles at further distances from the boundary. The mapped particle intensity distributions consequently become strongly elliptical in the vertical (or horizontal) direction, biasing the outcome of the correlation operator as illustrated in figures 9(b), (c) and (e)<sup>2</sup>.

This effect in itself is detrimental to the accuracy attainable with image mapping and any subsequent error analysis would as a result disfavour image mapping. Instead, to enable an objective evaluation of the overall applicability of image mapping, the authors present a fix to reduce this unfavourable effect. The authors propose a more robust approach involving image re-sampling of logical pixels prior to cross-correlating whereby the image mapping is performed on the basis of individual interrogation windows using an independent number of sampling points. As the process involves a transformation of the various units between the physical and logical plane, table 1 summarizes main related definitions to assist the reader, which are graphically clarified in figure 8.

Strongly curved meshes distort the shape of the particle images as illustrated in figures 9(a) and (b). The stretched particle images (figure 9(c)) create a distorted correlation map (figure 9(e)) and negatively affect the mapping-related bias error as argued by Ronneberger *et al* (1998). To this extent, a re-sampling process is introduced. Starting from a logical rectangular interrogation window, whose sizing will be covered in section 4.4, the radial and angular dimensions of its mapped equivalent in the physical plane are evaluated in terms of physical pixel units. This yields a length  $\gamma_k$  (in physical pixels) for each curvilinear side  $k$  of the physical window. To maintain the circular shape of the particle

images in the logical plane, the number of mapped pixels  $N_\xi$  and  $N_\eta$  along the tangential and radial directions respectively within each logical correlation window is then selected automatically considering these extents:

$$N_\xi = \frac{1}{2}(\gamma_{\text{top}} + \gamma_{\text{bottom}}) \text{ and } N_\eta = \frac{1}{2}(\gamma_{\text{left}} + \gamma_{\text{right}}). \quad (5)$$

The enhanced resampling thus re-evaluates the number of logical pixels dividing the logical, rectangular shaped correlation window ensuring a sufficient number of pixels to produce equally stretched particles in the horizontal and vertical direction (figure 9(d)). The shape of the particles in the mapped windows is consequently preserved yielding symmetric correlation peaks (figure 9(f)). The improvement can also be shown by evaluating a Gaussian fit of the correlation peaks, shown in figures 9(e) and (f), and evaluating the ratio between the horizontal and vertical widths. This ratio equals 5.2 for a constant sampling and 1.2 for the re-sampled correlation window, illustrating the improved correlation symmetry. Image intensities within the logical pixels are retrieved by quintic spline interpolation (Astarita and Cardone 2004) of the original intensity distribution in the corresponding physical locations obtained by forward mapping (Wolberg 1990). The reader should note that these logical pixels, which are arranged in a Cartesian manner in the logical plane (red circles in figure 8(a)) can consist of several logical units (figure 8(a)).

The outcome of the subsequent cross-correlation operation on the logical interrogation areas yields a displacement quantified in terms of logical pixels. These in turn depend on the number of imposed (re-) sampling points expressed in (5), necessitating a rescaling prior to the Jacobian-based conversion of displacements from the logical plane to the physical plane (see equation (4)). The conversion from logical pixels into logical units, for each displacement, is given by:

$$u_{\xi,\eta} = u_{\xi,\eta}^* \frac{WS_{\xi,\eta}}{N_{\xi,\eta}}. \quad (6)$$

Subscripts denote consideration of either the tangential  $\xi$  or radial direction  $\eta$ ,  $u_{\xi,\eta}$  represents the displacement converted into logical units,  $u_{\xi,\eta}^*$  symbolises the displacement in logical pixels resulting from the correlation in the logical plane and  $WS_{\xi,\eta}$  indicates the extent of the window in the logical plane in terms of logical units. The determination of  $WS_{\xi,\eta}$  will be discussed in section 4.4.

<sup>2</sup> An example of the bias error in case of a polar-Cartesian transformation is provided in figure 14.

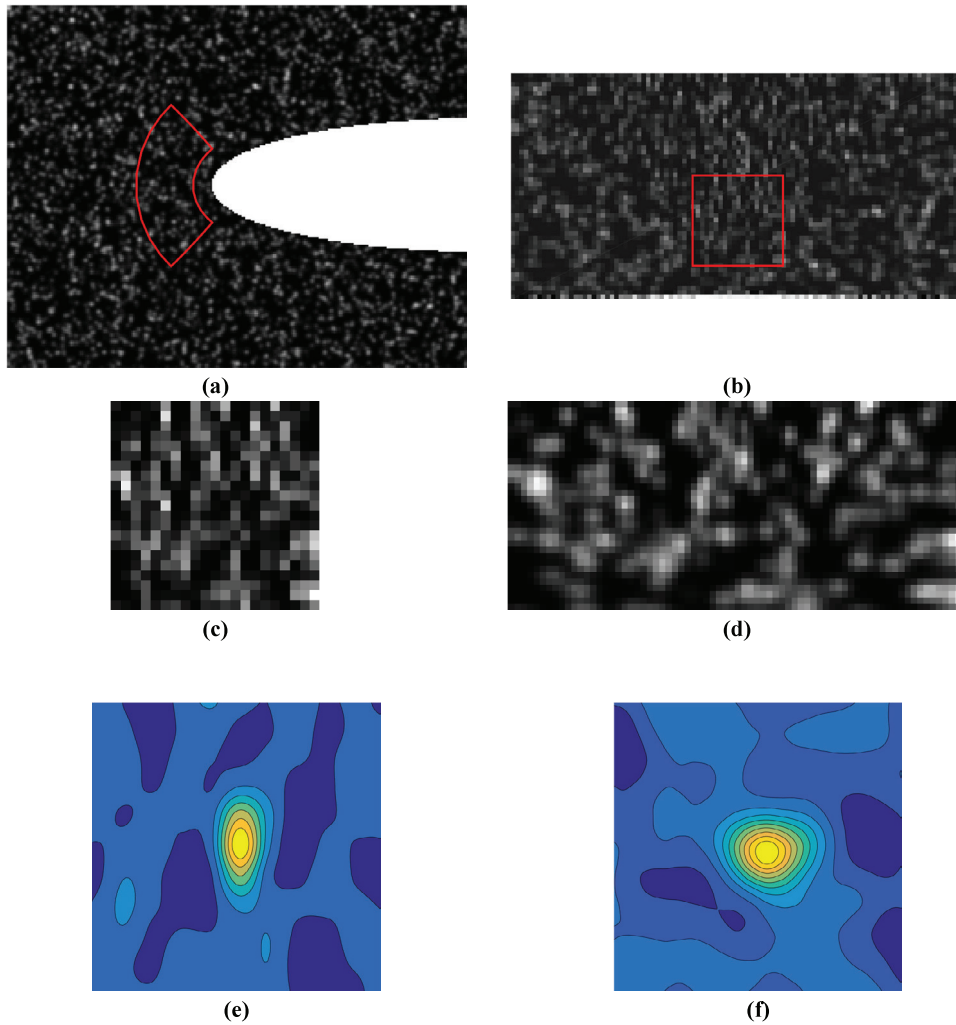


**Figure 9.** (a) Effect of the enhanced resampling for the case of the leading edge of a Joukowski airfoil shape. (b) The same correlation window is shown on the logical plane. (c) Logical correlation window adopting constant sampling and (d) the enhanced resampling showing the effectiveness of the method. Exemplary cross-correlation maps in case of (e) constant sampling and (f) enhanced resampling. Enhanced resampling improves the circularity of the particle images and correlation peak symmetry.

4.4. Interrogation window sizing on the logical plane

Contrary to standard PIV algorithms, interrogation window sizing during the process of image mapping is more complicated due to the non-linear correspondence between physical and logical interrogation window sizes:

$$\begin{bmatrix} WS_\xi \\ WS_\eta \end{bmatrix} = [J(x, y)]^{-1} \begin{bmatrix} WS_x \\ WS_y \end{bmatrix} \quad (7)$$

where  $WS_x$  and  $WS_y$  are the horizontal and vertical window sizes on the physical plane. Variables  $WS_\xi$  and  $WS_\eta$  depict the angular and radial sizes respectively on the logical plane. This dependency was already highlighted in section 4.3 in the context of particle image distortions. As per equation (7), due to the spatial dependency of the Jacobian, equally sized correlation windows in the physical plane will yield non-uniform window sizes in the logical plane and vice versa. This problem has never been clearly stated in existing literature and the authors accordingly propose two different solutions to automatically adjust the size and the position of the correlation windows on the logical plane.

**Table 1.** Definition of main units used in the description of correlation in the logical plane.

Physical pixel	:	The standard picture element, i.e. pixel, of the (original) image in the physical plane
Logical/mapped pixel	:	The picture element of the image mapped onto the logical plane
Logical unit	:	Radial and angular units in the logical plane defined by the numerical mapping

The first implementation, referred to as (straightforward) image mapping (IM), involves a recursive re-evaluation of interrogation area size and position on the logical plane in order to maintain the significance of the imposed window size. Once interrogation windows are distributed on the physical plane as per standard PIV (figure 10(a)) and selected spatial locations are transformed from physical to logical coordinates using the inverse mapping functions  $\xi(x, y)$  and  $\eta(x, y)$  (section 4.2, figure 10(b)), window sizes are converted from physical pixels into logical units using equation (7). This yields the logical window sizes  $WS_\xi$  and  $WS_\eta$  which appear in equation (6)



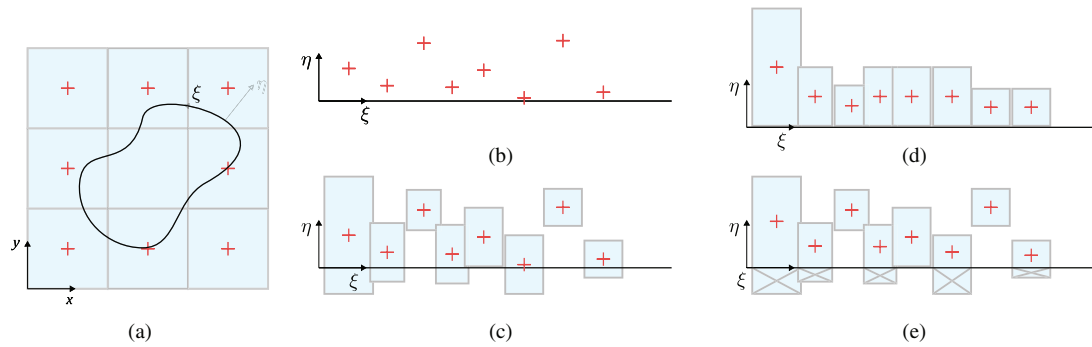


**Figure 10.** Iterative window repositioning and sizing in the logical plane. (a) Correlation windows are located in the physical plane and (b) their centroids are mapped into the logical plane. (c) Window sizes are based on the Jacobian of the coordinate transformation at the corresponding window centres, potentially causing overlap with the interface boundary. (d) Logical windows are relocated and re-evaluated in size until no residual overlap with  $\eta = 0$ . (e) Logical window areas extending below  $\eta = 0$  are ignored and vectors are relocated to the centre of the reduced window.

(figure 10(c)). As per the original aim of applying image mapping to avoid any overlap between correlation windows and identified interfaces, logical interrogation windows are then shifted to avoid overlap with the horizontal line at  $\eta = 0$  referencing the interface boundary (figure 10(d)). The shifted logical positions correspond with new values of the Jacobian and therefore new window sizes on the physical plane. Window dimensions on the logical plane are then re-calculated and the process is repeated until none of the correlation windows extends below  $\eta = 0$ . This is typically satisfied in only 2 iterations.

The second implementation of the window sizing algorithm, known as image mapping with vector relocation (IMVR), is a modification of IM, taking advantage of the vector relocation technique (Usera *et al* 2004). Correlation windows in the logical plane are now allowed to exhibit a certain degree of overlap with  $\eta = 0$  and, contrary to shifting the window in its entirety, are cut-off followed by a repositioning of the resulting velocity vector. The first steps of the second approach thus remain identical to those of the IM method (figures 10(a)–(c)). In IMVR, the portion of those correlation windows extending below  $\eta = 0$  is now masked from the process of cross-correlation and the resulting vector is consequentially relocated in the centre of the remaining area (figure 10(d)).

#### 4.5. Computational expense

It is clear that the combination of the additional operations underpinning image mapping must come at some elevated computational cost. A distinction can be made between one-off additional effort for the generation of the numerical mesh throughout the multi-grid interrogation process and a persistent one due to the mapping of particle images (figure 10). The mesh is generated once and remains invariant in case of stationary interfaces whereas the repeated effort related to the mapping, instead, cannot be prevented. The PIV image could be deformed in its entirety only once before the analysis. However the authors strongly discourage the reader to take this approach, especially when highly curved surfaces are considered due to the resulting strongly deformed particle images (figures 9(c)–(e)). The suggested solution of enhanced re-sampling (figures 9(d)–(f)), on the other hand, requires the interpolation of both numerical mesh data and image grey

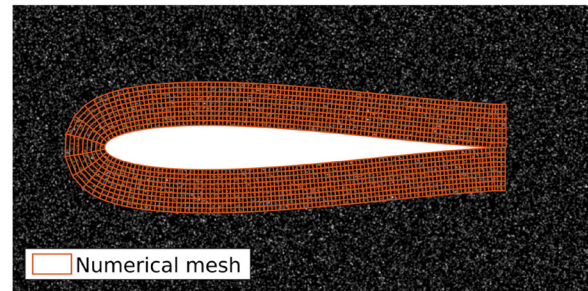


**Figure 11.** Sample of PIV image for the Joukowski aerofoil depicted with the numerical mesh (down-sampled for illustration purposes) used for the image mapping.

levels for every interrogation area. Although this process can be quickly accomplished by means of quintic splines, it nevertheless typically augments the overall processing time by 3 to 6 times the time spent on the cross-correlation operator, depending on the density of the numerical mesh and its wall-normal extent. This additional load, however, only applies to the Chimera region where image mapping is involved and does not affect all the correlation windows.

## 5. Numerical assessment

To discern advantages and disadvantages of the image mapping process and associated inherent errors, methodic analyses have been performed on the basis of numeric simulations. Three different error analyses are presented to investigate every aspect involved in the application of image mapping to PIV. The first analysis, presented in section 5.1, investigates the errors originated by the use of a numeric mesh in the conversion of points and vectors and does not involve any use of images or cross-correlation. The mesh adopted for this study was generated around a strongly curved Joukowski aerofoil and is depicted in red in figure 11. In section 5.2, attention is focussed on the effect of the deformation of particle images on bias and random error. Therefore a single correlation window for a flow around a cylinder is analysed with cross-correlation and a simple analytical transformation is adopted for the image mapping. Finally, section 5.3 investigates the error involved in the application of image mapping to a full PIV algorithm, juxtaposing the obtained particle image displacement estimates with alternative



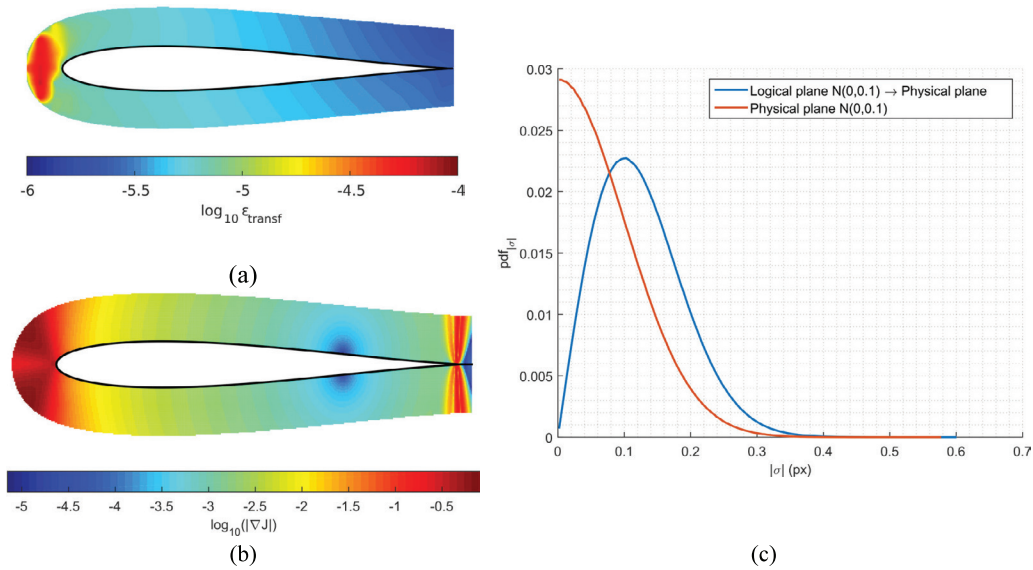


**Figure 12.** (a) Numerical error in mesh transformation, in log10 scale, after sequential coordinate transformation (physical plane  $\rightarrow$  logical plane  $\rightarrow$  physical plane). (b) Magnitude of the gradient of the coordinate transformation's Jacobian. (c) Amplification of random displacement error in the logical plane originating from coordinate transformation.

advanced techniques for measurements close to surfaces. For this analysis, the Joukowski aerofoil from section 5.1 is re-used to generate a set of synthetic images (figure 11) together with the numerical mesh used for the image mapping process.

### 5.1. Inherent error source 1: mesh interpolation and displacement transformation

Independent of the adopted numerical mesh, the transformation from physical to logical plane must be carried out through an interpolation (see section 4.2). Without regard to the PIV algorithm in which image mapping is implemented, this inherently produces a numerical error for both vector components and locations when converted and is non-negligible although often overlooked in existing literature. Quantification of this error is not straightforward though because of the lack of explicit analytical expressions specifying the transformations. The authors have therefore performed a simplistic analysis by consecutive mapping of spatially distributed points from the physical plane to the logical plane (inverse transformation) and back (direct transformation) as shown in figure 7. The error heuristic,  $\epsilon_{\text{transf}}$ , is then defined as the difference between the initial point locations and their doubly-converted position, as expressed by:

$$\epsilon_{\text{transf}} = \left\| \begin{array}{l} x^*(\xi^*(x_k, y_k), \eta^*(x_k, y_k)) - x_k \\ y^*(\xi^*(x_k, y_k), \eta^*(x_k, y_k)) - y_k \end{array} \right\| \quad (8)$$

where  $x^*(\cdot)$ ,  $y^*(\cdot)$  and  $\xi^*(\cdot)$ ,  $\eta^*(\cdot)$  are respectively the interpolation of the numerical solutions for the physical and logical coordinates of the mesh, as described in section 4.2, and  $x_k$  and  $y_k$  are sampling points distributed over the physical plane. The contour of  $\epsilon_{\text{transf}}$  is depicted for a hyperbolic mesh generated over a Joukowski aerofoil in figure 12(a), in logarithmic scale.

The observed error with regard to distribution and magnitude is conservative as it considers both errors originating

from the direct and inverse transformations, with the latter being less accurate due to the scattered nature of the required interpolation (see section 4.2). In reality, the two transformations are never used consecutively, for which reason this result must be considered as an upper error limit. Figure 12(a) illustrates the maximum expected error in the vector position to be less than  $10^{-3}$  pixels, i.e. one order of magnitude below the commonly accepted limit in displacement accuracy ( $\sim 0.01$  pixels) obtainable with standard PIV (Huang *et al* 1999). Nevertheless, figure 12(a) shows that highest errors in transformation are encountered in proximity of the leading edge. The reader is reminded that this error analysis is independent from the PIV analysis as it only originates from the mapping of points using the mesh transformation. However, this general tendency is independent of the mesh density (see section 4.1) and is related to the divergence of the characteristic mesh lines in presence of surface curvature. The digression of the lines is evidenced by the strong derivatives of the Jacobian shown in figure 12(b), which increase in magnitude as the distance from the aerofoil increases. The same effect can be observed on the trailing edge too, where mesh lines are instead converging. Unfortunately, this additional error will occur exactly where velocity gradients and image deformation are stronger, contributing overall to a deterioration of the measurement accuracy in these regions.

Mapping of velocity components, in theory, should be less prone to error than mapping of points, as it involves a simple rearrangement of equation (4). The Jacobian in this equation is evaluated using derivatives of the structured mesh data on the logical plane and this step is therefore more accurate than the inverse transformation of the points, with negligible error throughout the entire PIV algorithm. However, the conversion of velocity components is affected by a different source of error which is not related to the interpolation but rather to an amplification of the standard PIV error connected to the use of the Jacobian itself. This amplification can be

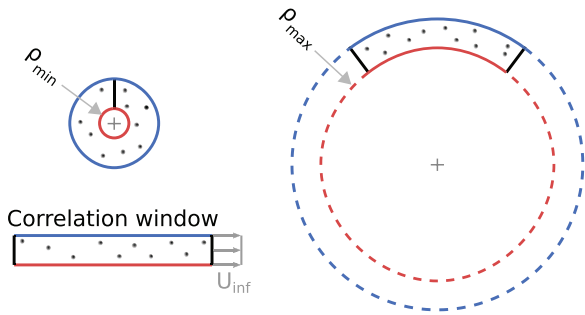


**Figure 13.** Description of the assessment of mesh-curvature influence. The correlation window size is chosen according to the circumference of the circle of smallest radius.

easily illustrated by considering a simple polar to Cartesian transformation;  $x = \rho \cdot \cos(\theta)$  and  $y = \rho \cdot \sin(\theta)$ . When the displacement field on the logical plane is subjected to an error  $\varepsilon_{\log}$ , the transformed error on the physical  $\varepsilon_{\text{phy}}$  scales with radial distance

$$\begin{aligned} \begin{bmatrix} dx \\ dy \end{bmatrix} + \varepsilon_{\text{phy}} &= \begin{bmatrix} \cos(\theta) & -\rho \sin(\theta) \\ \sin(\theta) & \rho \cos(\theta) \end{bmatrix} \left( \begin{bmatrix} d\rho \\ d\theta \end{bmatrix} + \varepsilon_{\log} \right) \\ &= [J] \begin{bmatrix} d\rho \\ d\theta \end{bmatrix} + [J] \varepsilon_{\log} \rightarrow \|\varepsilon_{\text{phy}}\| = \|\varepsilon_{\log}\| \sqrt{1 + \rho^2}. \end{aligned} \quad (9)$$

In case of the Joukowski aerofoil, the norm of the Jacobian is depicted in figure 12(b) and a similar amplification of the error is observed in figure 12(c). Here, an artificially imposed probability density function of the magnitude of normally distributed random noise,  $\sigma$ , with a standard deviation of 0.1 pixels was superimposed on to the ideal velocity field near the Joukowski aerofoil's leading edge on the physical plane. When the same noise is superimposed to ideal displacements on the logical plane and converted back into the physical plane, noise is amplified by a factor 1.6 (figure 12(c)). The reader is reminded that this error amplification is independent of the PIV algorithm used, but is related to the geometry of the mesh adopted for image mapping. This error source may affect the quality of the measurements, especially in regions of stronger mesh curvature, thus limiting the general application of image mapping to PIV. Even if no other cause of mesh-related error was present, a random noise of a measurement will be amplified according to the mesh curvature simply because of the use of image mapping.

### 5.2. Inherent error source 2: mesh curvature influence on the particles distortion

When implementing image mapping within a PIV image interrogation process, special attention must be paid to the distortion of particle images as these establish the signal for cross-correlation. In line with findings reported in the previous paragraph, this error source will be strongly dependent on the mesh arching. To isolate and quantify the source of measurement inaccuracy pertinent to the mesh curvature, a special test case was designed using synthetic images. A single correlation window was deformed using a Cartesian  $(x, y)$  to polar  $(\rho, \theta)$  transformation around a cylinder of variable radius  $\rho$ , ranging

from 10 ( $\rho_{\min}$ ) to 700 pixels ( $\rho_{\max}$ ). To nullify the influence of velocity gradients, a constant shift of 1.25 logical pixels was imposed along the  $\theta$ -axis in the logical plane. Using the Jacobian in equation (4) with conventional polar coordinate transformations corresponding displacements in the physical  $(\delta x, \delta y)$  and logical plane  $(\delta \rho, \delta \theta)$  were expressed as

$$\begin{cases} \delta x = -U_{\text{inf}} \rho \sin(\theta) \\ \delta y = U_{\text{inf}} \rho \cos(\theta) \end{cases} \quad \text{and} \quad \begin{cases} \delta \rho = 0 \\ \delta \theta = U_{\text{inf}} = 1.25 \end{cases} \quad (10)$$

To decouple the error due to particle deformation from other effects connected to image mapping, the size of the interrogation window on the logical plane was kept constant while testing multiple cylinder radii (see figure 13). The logical height of the window  $WS_{\rho}$  was arbitrarily set to 35 logical pixels, while the logical width  $WS_{\theta}$  was based on the largest angular extent (i.e. the circumference) of the minimum radius tested;  $WS_{\theta} = 2\pi\rho_{\min} \approx 63$ . Physical particle images were thus sampled using a constant number of logical pixels.

However, as the physical extent of logical pixels depended on their radial location within the correlation window, particle images were resampled following a 1:1 ratio nearest to the cylinder radius (i.e. one logical pixel per physical pixel) and under-sampled by a factor  $1 + 35/\rho$  furthest. Accordingly, this test allowed assessing solely the effect of elliptical warping due to mesh curvature. Bias and random errors in measured displacement, noted as  $\beta$  and  $\sigma$  respectively, for different particle diameters following Monte-Carlo simulations involving  $10^4$  synthetic images are plotted against the cylinder radii in figure 14. The error for a correlation window of the same size, non-deformed (i.e. infinite cylinder radius), shifted by the same rigid displacement, is also depicted for comparison as a dashed line.

A strong dependency between error and cylinder radius can be observed in both figures 14(a) and (b). Comparing the undeformed (dashed lines) with the deformed bias error (solid lines), figure 14(a) indicates the implementation of image mapping to augment the displacement bias error. Independent of the particle image diameters, this additional bias error can be up to  $8 \cdot 10^{-3}$  pixels in case of the strongest deformation tested (i.e. minimum cylinder radius) and decreases monotonically as the cylinder radius increases, reaching a minimum of  $8 \cdot 10^{-4}$  pixels for the maximum radius tested. This behaviour is to be expected as the size of the cylinder affects the deformation of the particle images, increasing their elliptical shape. For all the particle diameters analysed, results are in accordance with the existing literature, with smaller particle diameters presenting a higher bias error, as they tend to degrade the accuracy of correlation peak sub-pixel fitting (Westerweel 2000). Inspection of figure 14(b) reveals a similar behaviour for the random error, with image mapping introducing an additional error in the measurements inversely proportional to the cylinder radius. For cylinder radii exceeding 100px random errors increase with particle image diameter. In case of strong deformations a rapid increase in random error can be observed for the smaller particle image diameter, yielding error levels exceeding those for larger diameters. The discrepancy between the asymptotic behaviour of the curves shown

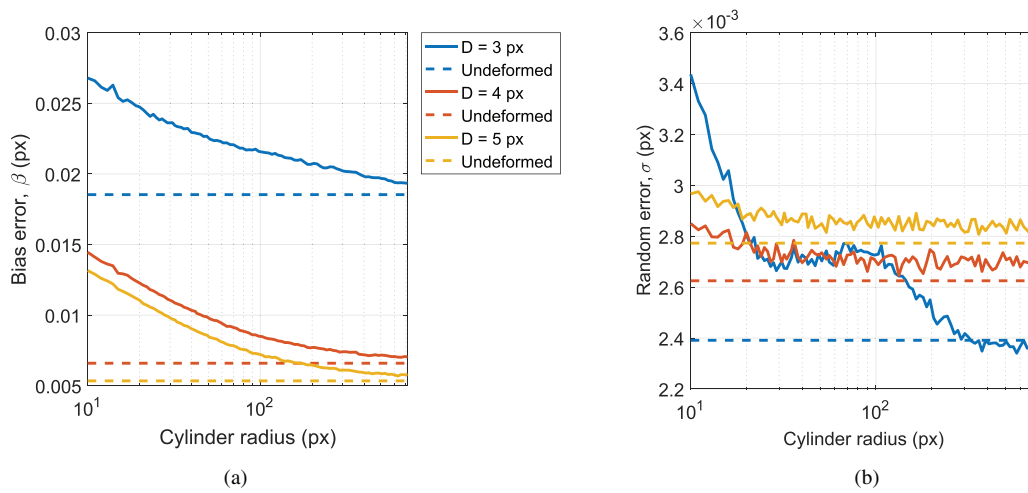


**Figure 14.** (a) Bias error  $\beta$  and (b) random error  $\sigma$  in measured particle image displacement versus cylinder radius with varying particle image diameter. Dashed line represent errors for cylinders of infinite radius.

**Table 2.** Interrogation procedures considered in image interrogation performance assessment.

	ASVR	ASIM	ASIMVR	CSV	CSIM
Correlation window distribution	Adaptive (AS)	Adaptive (AS)	Adaptive (AS)	Cartesian (CS)	Cartesian (CS)
Image mapping	No	Yes (IM)	Yes (IM)	No	Yes (IM)
Vector relocation	Yes (VR)	No	Yes (VR)	Yes (VR)	No

in figure 14 and the corresponding reference cases is due to numerical errors originating from the different interpolation processes intrinsic to image mapping.

The authors would like to stress the fact that the mapping was here defined analytically. Presented errors in this subsection therefore reflect the influence of mesh curvature only and not mesh type. When using image mapping, a decrease in the measurement accuracy can thus be expected where mesh curvature is stronger merely due to the particle image deformation. Notwithstanding, actual advantages of image mapping will be case dependent (geometry shape, mesh type, flow gradients, correlation window distribution, etc) and may outweigh the above error.

### 5.3. Limits of image mapping in a complete PIV analysis

In this section, image mapping has been embedded within PIV image analysis processes and compared with alternative advanced PIV interrogation routines. Numerical simulations presented afore have indicated measurement errors in particle image displacement, inherent to image mapping, to be strongly affected by the mesh curvature. To assess the limits of applicability of image mapping and investigate the maximum extent of these errors, a Joukowski aerofoil characterized by a strongly curved surface was therefore selected as a test case representative of aeronautical applications. Synthetic images were generated with seeding consisting of randomly distributed Gaussian shaped particle images with diameters selected from a normal probability (3 pixels mean, 1 pixel variance) and a concentration of 0.1 particles per pixel. Images had a bit depth of 8 with mean particle intensities of 120 and standard deviation of 40 grey levels. The analytical inviscid

flow around a Joukowski airfoil enabled the direct evaluation of resulting measurement errors in case of realistic aerodynamic shapes containing regions of high surface curvature.

Five combinations of image interrogation procedures (summarised in table 2) have been tested for different settings such as interrogation window size, number of predictor-corrector iterations and image noise. The algorithms combined different implementations of correlation window distributions, vector relocation and image mapping. Being the measurement in the near vicinity of the object the main interest of this paper, the authors focused their attention on the implementation of image mapping combined with an adaptive sampling distribution as proposed by Theunissen *et al* (2008b). For this implementation, formally referred to as adaptive sampling (AS), correlation windows are adaptively located to allow an automatic selection of the window properties. The density of correlation windows increases automatically towards the interface, with a consequent increase in windows overlap too, as depicted in figure 20(a). The combination of adaptive sampling and vector relocation (Usera *et al* 2004), whereby no use is made of image mapping, will be referred to as ASVR (adaptive sampling vector relocation). This approach will serve as a basis for the comparison of the performances with more advanced techniques. The image mapping algorithm, as described in section 4.4, can be implemented with or without vector relocation, yielding the ASIM (adaptive sampling image mapping, see figure 10(d)) and ASIMVR (adaptive sampling image mapping with vector relocation, see figure 10(e)) approaches. An adaptation of the algorithms on a standard Cartesian grid is also proposed for the sake of comparison, referred to as CSV (cartesian

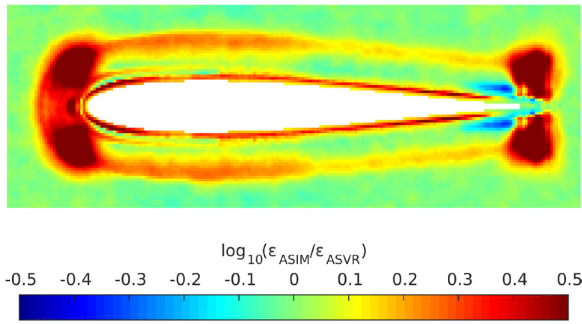


**Figure 15.** Comparison of displacement error between ASIM and ASVR. Number of iterations: 3. Correlation window size: 90 → 25. No image noise.

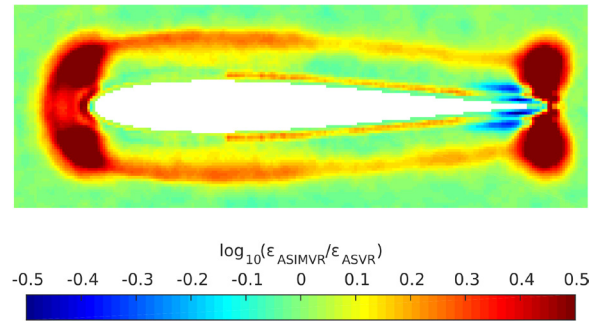


**Figure 16.** Comparison of displacement error between ASIMVR and ASVR. Number of iterations: 3. Correlation window size: 90 → 25. No image noise.

sampling vector relocation) and CSIM (cartesian sampling image mapping). An overview of the conceptually different methodologies is provided in table 2.

In the following, plots depict the total measurement error  $\varepsilon$  averaged over 1000 synthetic images. For each velocity field the reconstruction error is quantified by interpolating the measured displacements,  $dx_m$  and  $dy_m$ , on a pixel-wise grid and evaluating the difference with the theoretical, analytical, displacements,  $dx_a$  and  $dy_a$ , in the corresponding location;  $\varepsilon = ((dx_m - dx_a)^2 + (dy_m - dy_a)^2)^{0.5}$ . To ease comparison between the different interrogation approaches, the ratio between errors is presented on a logarithmic scale;  $\log_{10}(\varepsilon_{ASIM}/\varepsilon_{ASVR})$ ,  $\log_{10}(\varepsilon_{ASIMVR}/\varepsilon_{ASVR})$ , and  $\log_{10}(\varepsilon_{CSIM}/\varepsilon_{CSVR})$ . Values close to zero indicate the two methods to have the same performances (error near unity ratio). This can be expected outside the Chimera area where no image mapping is invoked and differences between methodologies are marginal.

In the absence of image noise, figure 15 shows the comparison of the error between ASIM and ASVR performed in 3 predictor-corrector iterations with window sizes reduced from 90 to 25 pixels. The spatial distribution in error presents patterns which can be attributed to the process of image mapping and to the characteristics of the numerical mesh. Starting from the leading edge, the highest error is concentrated in two agglomerations above and below the aerofoil. In these areas the Jacobian of the mesh reaches its maximum (figure 12(a)), amplifying random fluctuations of the velocity field and increasing the error as described in section 5.2. Moreover, due to the low radius of curvature of the aerofoil (10 pixels), this image area is affected by the strongest particle deformation and an additional error in terms of bias and random is expected, as already shown in figure 14.

On the edge of the airfoil ASIM persistently attains a higher error. This consistent behaviour highlights an obstacle to the application of image mapping which has never been addressed in literature before. In fact, ASIM maintains the interrogation window size constant in proximity of a boundary and, as a consequence, the minimum distance between a displacement vector and the aerofoil boundary is at least half the minimum window size. Conversely, with ASVR vectors are repositioned to the centre of gravity of the correlation window portion occupied by the seeded flow. This yields a minimum distance of one-quarter of the minimum window size. Moreover, due to the lack of noise in the synthetic images, smaller interrogation

windows are always associated to a smaller error. ASVR, whereby parts of the correlation windows overlapping with the aerofoil are masked automatically, results in analysing correlation windows which are smaller than the minimum set by the user. Therefore, in this particular case, ASVR produces better vectors which are closer to the aerofoil. It will be shown that in the presence of image noise this reasoning no longer holds.

Moving to the aft of the aerofoil, a behaviour in error similar to the leading edge is noticeable on the trailing edge. In proximity of the edge, a strong reduction in error is achieved with ASIM, yet accuracy rapidly reduces. The observed behaviour can be explained considering three different phenomena; the process of window repositioning on the logical plane described in section 4.4; the adaptive point distribution and the interpolation effect of the predictor-corrector implemented in the algorithm. As already described in section 4.4, correlation windows on the logical plane are automatically repositioned in order to keep the seeding density constant and to ensure they all have exactly the same area. This process inevitably produces a clustering of sampling points on the edges of the Chimera region, as shown in figure 20. During the predictor-corrector process, the interpolation of velocity data in those areas of higher data density will produce a lower error of the velocity predictor and consequently a final error of ASIM which is lower than ASVR. The reader is reminded that this lower error is not related to the enhancement of the images produced by image mapping itself but rather to a mere effect of the interpolation due to the inherited clustering of data points.

The only difference between the implementation of image mapping in ASIM and ASIMVR is encountered near the airfoil edge (figure 16). ASIMVR does not shift the window position to keep the area constant, but in an analogous way to ASVR, masks the correlation window area overlapping with the aerofoil on the logical plane and relocates the vector in the centre of gravity of the captured flow region. The effect shows an error of ASIMVR on the edge of the aerofoil which is on par with ASVR. In this case the application of image mapping results in no improvement of the measurement accuracy. However, it is important to stress that this result is only valid for the ideal case of images without artificial noise. The ASIMVR algorithm does not produce any clustering of points since no repositioning of logical windows is performed.



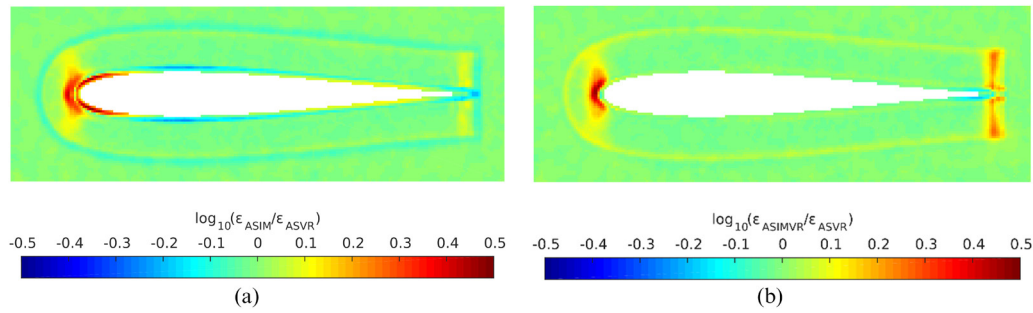


**Figure 17.** Comparison of displacement error between (a) ASIM and ASVR, (b) ASIMVR and ASVR. Number of iterations: 3. Correlation window size:  $90 \rightarrow 25$ . With image noise.

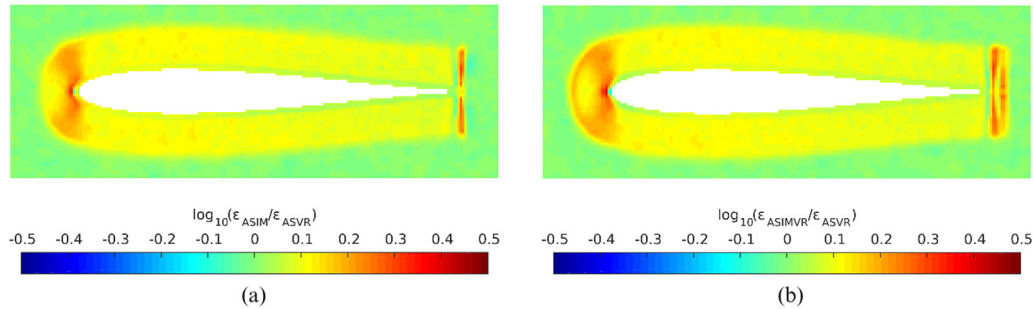


**Figure 18.** Comparison of displacement error between (a) ASIM and ASVR, (b) ASIMVR and ASVR. Number of iterations: 1. Correlation window size: 25. With image noise.

Nevertheless, comparison of figure 16 with figure 15 indicates a noticeable reduction of displacement error near the trailing edge. Despite the minimum interrogation window size imposed by the user, the actual area adopted by ASIMVR for the cross-correlation depends of many different conditions. On the trailing edge, the numerical mesh is logically cut along the aerofoil chord as shown in figure 11. Because of this discontinuity, interrogation windows close to the trailing edge analysed with ASIMVR will be smaller than windows positioned in the same area but analysed with ASVR. In absence of noise, this produces a smaller error for ASIMVR.

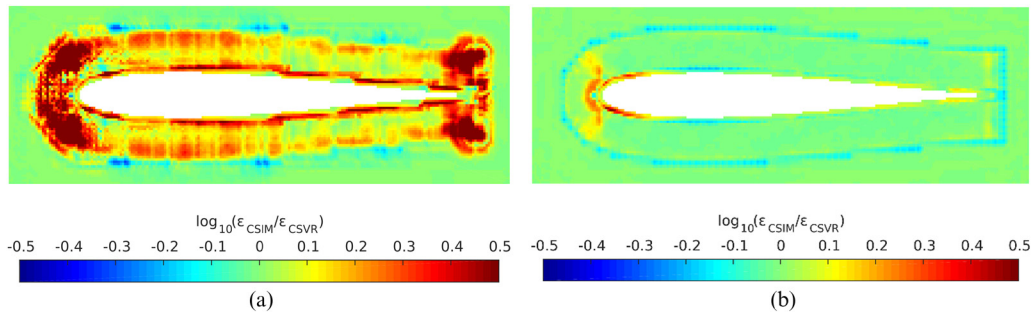
With the purpose of understanding all the possible advantages and applications of image mapping, and proposing a more realistic case of images, the previous analysis has been repeated in the presence of artificial noise, in the form of a normal distribution with mean of 2.8% and standard deviation of 3.6% of the maximum intensity, added to the ideal images. The spatial distribution in displacement error produced by image mapping or standard adaptive PIV algorithms presents many similarities with the two previous cases. Now the relative importance of the error produced by the mesh transformation is dominated by the uncertainty brought by the artificial noise. Differences inherent to the image mapping technique are amplified accordingly.

Figure 17(a) presents the error ratios between ASIM and ASVR and shows features of high error similar to those in figure 15. These are again due to the strong deformations in the numerical mesh. However, a remarkable reduction in error with ASIM can be noticed in proximity of the aerofoil boundary. Because of the presence of artificial noise, a smaller window size, such is the case in ASVR, does not necessarily produce a better quality vector. Consequently, ASIM is able to yield measurements with higher accuracy by ensuring that all

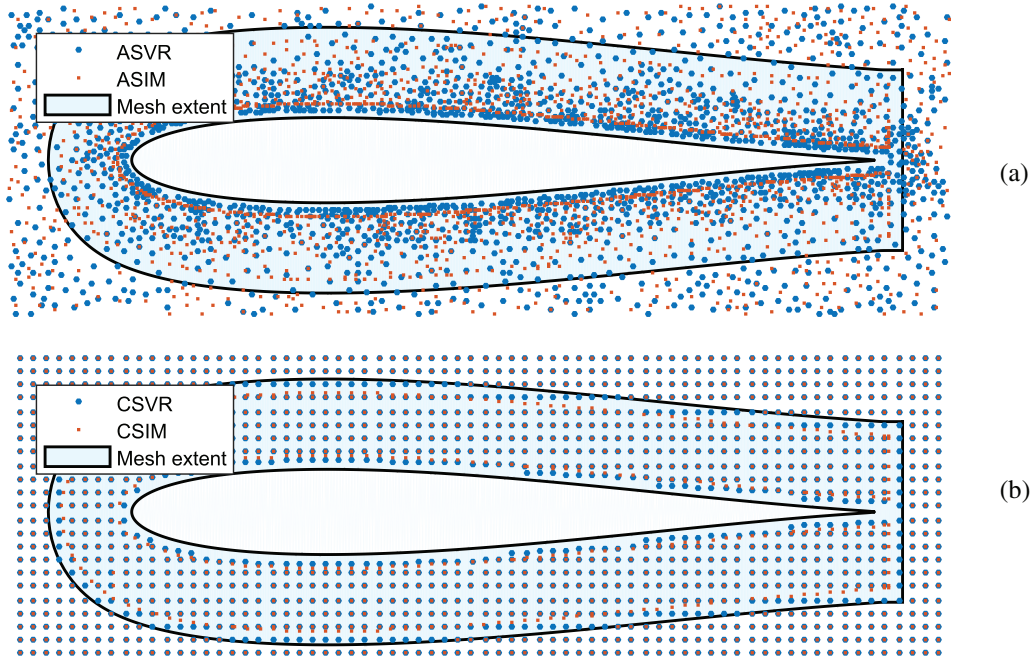
correlation windows respect the minimum window imposed by the user. This result is in accordance with the improvements already shown in literature (Jeon and Sung 2011) where a reduction of the error is expected in case of low curvature radius and images affected by artificial noise. Another area of smaller error in figure 17(a) is on the outer edge of Chimera which is ascribed to the higher density of sampling points.

Figure 17(b) shows the error ratio for ASIMVR and presents similar features to ASIM. Because of artificial noise, the inherent characteristic of using smaller windows, which was beneficial in absence of noise, now becomes harmful. For this reason, the error of ASIMVR on the edge of the aerofoil reaches levels on par with ASVR. The same reduction in window size on the trailing edge due to the logical cut of the mask worsens the measurement precision. For the same reason, the error present on the outer area of the Chimera region is now negatively affected by the reduced window size and shows an increased level in figure 17(b) compared to figure 17(a).

With the objective of deepening the understanding in the conduciveness of image mapping in PIV algorithms, the analysis of the Joukowsky images has also been performed considering a single iteration thereby negating the predictor-corrector process. To allow the use of small correlation window sizes while maintaining a sufficient number of particle images per window, the maximum flow velocity magnitude was reduced to 1 px. Results are shown in figure 18 for both ASIM and ASIMVR and present once again the typical patterns of the numerical mesh error. However, given the very strong reduction of the velocity gradient magnitudes due to the very small displacement, there seem to be no actual advantages in using image mapping anymore. In fact, in spite of the artificial noise, quasi-static correlation windows are rotated, stretched and deformed by the image mapping without bringing any



**Figure 19.** Comparison of displacement error between CSIM and ASVR. Number of iterations: 3. Correlation window size: 90 → 25. (a) No image noise, (b) with image noise.



**Figure 20.** Distribution of correlation windows' centres the first iteration for (a) ASVR and ASIM and (b) CSVR and CSIM. Only by vector relocation can data be collected even closer to the airfoil than with image mapping.

reduction in the gradients of the velocity field. This finding is in accordance with the results shown in figure 12(c); the mere application of the image mapping process to a static displacement field amplifies the random fluctuation increasing the displacement error.

For the sake of completeness, a comparison with a structured Cartesian grid is also presented in figure 19. The figure shows similar patterns to the previous adaptive sampling, with the only differences being patchy artefacts due to the non-uniform distribution of the sampling points. The reader should note that the previous analysis, based on the adaptive point distribution, does not depend on the type of sampling distribution adopted, but rather on the peculiar aspects of image mapping and its algorithmic implementations.

**5.4. Summary: feasibility of image mapping**

The numerical assessment has indicated the applicability of image mapping not to be as simple and straightforward as suggested in previous works (Nguyen *et al* 2010, Park *et al* 2015). Instead, the final outcome of the measurement strongly

depends on a case-by-case basis, including the geometric shape of the interface and details of the algorithmic implementation. Essentially, two dominant effects determine the degree to which image mapping can be beneficial; image deformation as a result of the imposed numerical mesh and the ability to maintain the image density in the vicinity of the object boundary.

Although the numerical mesh introduces a distortion of the particle images which is detrimental to the correlation accuracy as illustrated in figure 14, depending on the alignment of the numerical mesh with the flow streamlines, the resulting artificial displacement gradients can be either constructive or unfavourable. In case of the cylinder flow presented in figure 13 the mesh transformation straightens the curved streamlines in the logical plane, thereby minimising gradients. Contrarily, in the case of the Joukowski airfoil near the leading and trailing edge, the misalignment between the governing flow and imposed numerical mesh combined with the strong gradients in the Jacobian (figure 12) led to a consistent deterioration of the PIV accuracy. Unfortunately, these effects cannot be quantified *a priori* as the underlying flow field is exactly the subject of the analysis.

The results presented in section 5.3 attest that image mapping does not generally yield an increase in accuracy, even when incorporated in advanced algorithms. Instead, the results suggest more simplistic interrogation methodologies to outperform those including image mapping. Only for very specific imaging and flow conditions marginal improvements could be attained by implementing image mapping. In the near vicinity of the Joukowski airfoil the ability of image mapping to avoid any overlap between the interrogation areas and the object meant that a more reliable cross-correlation could be achieved in the presence of image noise (figures 17 and 19). However, this improvement was irrelevant in the absence of image noise (figures 15 and 16). The potential gain in resolution consequently depends on two factors. First, the quality of the PIV images in proximity of the edges (i.e. severity of reflections, intensity of image noise, concentration of seeding, etc). This can be partly influenced by adequate pre-processing methodologies (e.g. Mendez *et al* (2017)). Second, the final correlation window size, which will typically involve trial and error. If the user selects a too large size to ensure a reliable correlation, no gain will be noticeable due to a too coarse resolution. Should the user opt for a too small correlation window size, independent of the analysis approach, cross-correlation will yield sporadic vectors.

## 6. Conclusions

The analysis of PIV images in the vicinity of surfaces is typically hampered by a reduction in seeding density and the presence of light reflections, rendering the cross-correlation process unreliable. By constructing a body-conforming numerical mesh using the identified interface as boundary condition, overlap between interfaces and correlation windows can be completely eliminated. With image mapping intensity distributions are subsequently transformed into the curvilinear coordinate system converting the interface boundary into a straight line such that it can be excluded from the interrogation process, in theory circumventing the associated error.

Previous works have already shown the application of this method on relatively easy test cases, proving the feasibility of image mapping on sinusoidal-like surfaces and cylinders. However, the general applicability of image mapping for curved geometries has to the best of the authors' knowledge never been scrutinised, nor has the performance of image mapping ever been compared with alternative PIV interrogation methodologies. For these reasons the authors have provided in the present work an in-depth analysis of the feasibility of image mapping in PIV, from the generation of boundary conditions from logical masking images to the construction of numerical meshes through to the problematic of image re-interpolation. For each stage, all potential error sources have been investigated and substantiated by assessments on synthetic test cases. In addition, the authors have proposed improvements to negate some of the errors inherent to image mapping in an attempt to truly assess the general applicability of image mapping for PIV image analyses.

The generation of a proper numerical mesh for image mapping has been proven to be one of the most influential parts of the process. Divergence and convergence in characteristic mesh lines, quantified by the transformation Jacobian, not only introduces artificial displacement gradients in the mapped images, but also causes a distortion of the mapped particle images negatively impacting cross-correlation accuracy. To reduce adverse effects an enhanced resampling procedure has been suggested to restore the circular shape of mapped particle images. Nevertheless, besides errors originating from the coordinate interpolation inherent to image mapping, highly curved surfaces have been shown to introduce an additional bias error that, depending on the particle image diameter, can be strongly amplified times when the radius of curvature is as low as 10 pixels.

Numerical assessments involving the analytical flow around a Joukowski aerofoil have shown that image mapping can provide improvements in measurement accuracy only under very specific conditions. The ability to maintain a constant window size and seeding density in a correlation window in the vicinity of the aerofoil allowed a reduction of the error in the areas of the boundary characterized by a lower curvature. However, surfaces of high curvature are always affected by strong image deformation and image mapping should therefore be avoided in these cases. Moreover, error improvements were only found in the presence of artificial noise. This is to be expected since the increased error near surfaces is often due to a loss of seeding density and increase in background reflections. In absence of these circumstances, the advantages of using image mapping are strongly limited and a vector relocation technique, implemented in more standard and less computationally intense routines, could be sufficient for the analysis.

The benefit of image mapping was thus shown to be dependent on two specific conditions; the necessary alignment of the mesh lines with flow streamlines to avoid the generation of additional velocity gradients and adequate interrogation parameters near the object (correlation window size). These requirements have nearly always been fulfilled in existing literature adopting image mapping, which explains the relative success of the method. Both require *a priori* knowledge of the underlying flow field and optimal processing parameters, which are exactly the unknowns in the performed image analysis. Considering the increased computational cost and added sources of error, the potential gain from implementing image mapping in conventional PIV interrogation schemes must therefore be evaluated on a case-by-case basis. When dealing with strongly curved geometries or when streamlines are not parallel to the interface, image mapping is without doubt ineffective and methodologies invoking adaptive image processing or particle tracking will warrant more favourable results.

## Acknowledgment

This work has been funded by the UK's Engineering and Physical Sciences Research Council (EPSRC—EP/L010755/1). The authors greatly appreciate their support. All underlying data to support the conclusions are provided within this paper.



## Appendix. Numerical solution of the hyperbolic mesh equations

The relationship between physical coordinates  $(x, y)$  and logical coordinates  $(\xi, \eta)$  is expressed in (2) from which follows:

$$x_\eta = -\frac{\Delta A}{\lambda} y_\xi, \quad y_\eta = \frac{\Delta A}{\lambda} x_\xi \quad \text{with } \lambda = x_\xi^2 + y_\xi^2. \quad (\text{A.1})$$

By introducing a four-point stencil, the discrete values of  $x$  and  $y$  can be expressed as  $x_{i,j}$  and  $y_{i,j}$ , where the indices  $i$  and  $j$  depict the discrete location along the logical axis  $\xi$  and  $\eta$ . Following this approach, partial derivatives in (A.1) can be discretised using second order central differences:

$$\frac{x_{i,j+1} - x_{i,j-1}}{2\Delta\eta} = -\left(\frac{\Delta A}{\lambda}\right)_{i,j} \frac{y_{i+1,j} - y_{i-1,j}}{2\Delta\xi},$$

$$\frac{y_{i,j+1} - y_{i,j-1}}{2\Delta\eta} = \left(\frac{\Delta A}{\lambda}\right)_{i,j} \frac{x_{i+1,j} - x_{i-1,j}}{2\Delta\xi}$$

$$\text{with } \lambda_{i,j} = \left(\frac{x_{i+1,j} - x_{i-1,j}}{2\Delta\xi}\right)^2 + \left(\frac{y_{i+1,j} - y_{i-1,j}}{2\Delta\xi}\right)^2. \quad (\text{A.2})$$

The term  $\Delta A_{i,j}$  is defined as per (3). These equations can be rearranged to yield an expression for the unknowns  $x$  and  $y$  at the next value of the stencil in the marching direction  $\eta$ , i.e.  $(x_{i,j+1}, y_{i,j+1})$ , in terms of  $x_{i,j}$ ,  $y_{i,j}$ ,  $x_{i-1,j}$ ,  $y_{i-1,j}$ ,  $x_{i+1,j}$  and  $y_{i+1,j}$ . Starting from the solution on the boundary condition ( $\eta = 0$ ), the solution will thus propagate in the direction of increasing  $\eta$ .

## References

- Adrian R J 1991 Particle-imaging techniques for experimental fluid mechanics *Annu. Rev. Fluid Mech.* **23** 261–304
- Astarita T and Cardone G 2004 Analysis of interpolation schemes for image deformation methods in PIV *Exp. Fluids* **38** 233–43
- Bobach T, Farin G, Hansford D and Umlauf G 2009 Natural neighbor extrapolation using ghost points *Comput. Des.* **41** 350–65
- Chan W M and Steger J L 1992 Enhancements of a three-dimensional hyperbolic grid generation scheme *Appl. Math. Comput.* **51** 181–205
- Douglas D and Peucker T 1973 Algorithms for the reduction of the number of points required to represent a digitized line or its caricature *Can. Cartographer* **10** 112–22
- Feudjio C, Tiedeu A and Noubeg M 2014 Extracting and smoothing contours in mammograms using Fourier descriptors *J. Biomed. Sci. Eng.* **2014** 119–29
- Garcia D 2010 Robust smoothing of gridded data in one and higher dimensions with missing values *Comput. Stat. Data Anal.* **54** 1167–78
- Gui L, Wereley S T and Kim Y H 2003 Advances and applications of the digital mask technique in particle image velocimetry experiments *Meas. Sci. Technol.* **14** 1820–8
- Huang H, Dabiri D and Gharib M 1999 On errors of digital particle image velocimetry *Meas. Sci. Technol.* **8** 1427–40
- Jeon Y J and Sung H J 2011 PIV measurement of flow around an arbitrarily moving body *Exp. Fluids* **50** 787–98
- Keane R D and Adrian R J 1992 Theory of cross-correlation analysis of PIV images *Appl. Sci. Res.* **49** 191–215
- Masullo A and Theunissen R 2016 Adaptive vector validation in image velocimetry to minimise the influence of outlier clusters *Exp. Fluids* **57** 33
- Mendez M A *et al* 2017 POD-based background removal for particle image velocimetry *Exp. Therm. Fluid Sci.* **80** 181–92
- Nguyen C V, Nguyen T D, Wells J C and Nakayama A 2010 Interfacial PIV to resolve flows in the vicinity of curved surfaces *Exp. Fluids* **48** 577–87
- Nobach H and Honkanen M 2005 Two-dimensional Gaussian regression for sub-pixel displacement estimation in particle image velocimetry or particle position estimation in particle tracking velocimetry *Exp. Fluids* **38** 511–5
- Park J, Im S, Sung H J and Park J S 2015 PIV measurements of flow around an arbitrarily moving free surface *Exp. Fluids* **56** 56
- Paterna E, Moonen P, Dorer V and Carmeliet J 2013 Mitigation of surface reflection in PIV measurements *Meas. Sci. Technol.* **15** 1079–89
- Ronneberger O, Raffel M and Kompenhans J 1998 Advanced evaluation algorithms for standard and dual plane particle image velocimetry *Proc. of the 9th Int. Symp. on Applied Laser Techniques to Fluid Mechanics* pp 13–6
- Ruan X, Song X and Yamamoto F 2001 Direct measurement of the vorticity field in digital particle images *Exp. Fluids* **30** 696–704
- Scarano F 2002 Iterative image deformation methods in PIV *Meas. Sci. Technol.* **13** R1–19
- Scarano F and Riethmuller M L 2000 Advances in iterative multigrid PIV image processing *Exp. Fluids* **29** S051
- Steger J L 1991 The Chimera method of flow simulation *Workshop on Applied CFD* (University of Tennessee Space Institute)
- Theunissen R, Di Sante A, Riethmuller M L and Van Den Braembussche R A 2008a Confidence estimation using dependent circular block bootstrapping: application to the statistical analysis of PIV measurements *Exp Fluids* **44** 591–6
- Theunissen R, Scarano F and Riethmuller M L 2006 An adaptive sampling and windowing interrogation method in PIV *Meas. Sci. Technol.* **18** 275–87
- Theunissen R, Scarano F and Riethmuller M L 2008b On improvement of PIV image interrogation near stationary interfaces *Exp Fluids* **45** 557–72
- Thompson J F 1987 A general three-dimensional elliptic grid generation system on a composite block structure *Comput. Methods Appl. Mech. Eng.* **64** 377–411
- Thompson J F, Soni B K and Weatherill N P 1999 *Handbook of Grid Generation* (Boca Raton, FL: CRC Press)
- Tsuei L and Savaş Ö 2000 Treatment of interfaces in particle image velocimetry *Exp. Fluids* **29** 203–14
- Usera G, Vernet A and Ferré J A 2004 Considerations and improvements of the analysing algorithms used for time resolved PIV of wall bounded flows *Proc. 12th Int. Symp. on Applications of Laser Techniques to Fluid Mechanics (Lisbon, Port, 11–5 July)*
- Westerweel J 1997 Fundamentals of digital particle image velocimetry *Meas. Sci. Technol.* **8** 1379–92
- Westerweel J 2000 Theoretical analysis of the measurement precision in particle image velocimetry *Exp. Fluids* **29** S3–12
- Westerweel J 2008 On velocity gradients in PIV interrogation *Exp Fluids* **44** 831–42
- Wolberg G 1990 *Digital Image Warping* (Los Alamitos: IEEE Computer Society Press)